Biochar (2022) 4:37
https://doi.org/10.1007/s42773-022-00161-2

ORIGINAL RESEARCH

Insights into simultaneous adsorption and oxidation of antimonite [Sb(III)] by crawfish shell-derived biochar: spectroscopic investigation and theoretical calculations

Hanbo Chen[1,2,3] · Yurong Gao[1,2,3] · Jianhong Li[1] · Chenghua Sun[4] · Binoy Sarkar[5] · Amit Bhatnagar[6] · Nanthi Bolan[7,8] · Xing Yang[1] · Jun Meng[2,3] · Zhongzhen Liu[9] · Hong Hou[10] · Jonathan W.C. Wong[11] · Deyi Hou[12] · Wenfu Chen[2] · Hailong Wang[1,2,13]

Received: 6 April 2022 / Accepted: 24 May 2022

Abstract Removal of antimonite [Sb(III)] from the aquatic environment and reducing its biotoxicity is urgently needed to safeguard environmental and human health. Herein, crawfish shell-derived biochars (CSB), pyrolyzed at 350, 500, and 650°C, were used to remediate Sb(III) in aqueous solutions. The adsorption data best fitted to the pseudo-second-order kinetic and Langmuir isotherm models. Biochar produced at 350°C (CSB350) showed the highest adsorption capacity (27.7 mg g^{-1}), and the maximum 78% oxidative conversion of Sb(III) to Sb(V). The adsorption results complemented with infrared (FTIR), X-ray photoelectron (XPS), and near-edge X-ray absorption fine structure (NEXAFS) spectroscopy analyses indicated that the adsorption of Sb(III) on CSB involved electrostatic interaction, surface complexation with oxygen-containing functional groups (C=O, O=C–O), π–π coordination with aromatic C=C and C–H groups, and H-bonding with –OH group. Density functional theory calculations verified that surface complexation was the most dominant adsorption mechanism, whilst π–π coordination and H-bonding played a secondary role. Furthermore, electron spin resonance (ESR) and mediated electrochemical reduction/oxidation (MER/MEO) analyses confirmed that Sb(III) oxidation at the biochar surface was governed by persistent free radicals (PFRs) ($•O_2^-$ and •OH) and the electron donating/accepting capacity (EDC/EAC) of biochar. The abundance of preferable surface functional groups, high concentration of PFRs, and high EDC conferred CSB350 the property of an optimal adsorbent/oxidant for Sb(III) removal from water. The encouraging results of this study call for future trials to apply suitable biochar for removing Sb(III) from wastewater at pilot scale and optimize the process.

Graphical abstract

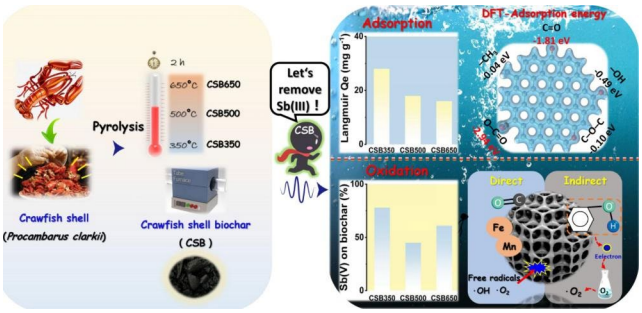

Article highlights

- Crawfish-shell biochar (CSB) pyrolyzed at 350°C showed the highest Sb(III) adsorption and oxidation.
- DFT calculations highlighted complexation, H-bonding and π–π interactions as key removal mechanisms.
- Sb(III) oxidation was mainly governed by persistent free radicals and electron transfer capacity of biochar.

Keywords Sorption · Heavy metal · Synchrotron · Density functional theory · Contaminated water

Extended author information available on the last page of the article

Published online: 04 July 2022

1 Introduction

Antimony (Sb) is a metalloid that belongs to Group VA of the periodic table, and the element exhibits chemical and bio-toxicological characteristics similar to arsenic (As), where oxyanions of both the elements might transform between trivalent and pentavalent species under variable redox conditions (Nishad and Bhaskarapillai 2021; Bolan et al. 2022b). Antimony exists in four oxidation states (-III, 0, +III, and + V) of which Sb(III) and Sb(V) are the prevalent forms in the environment, with Sb(III) 10-time more toxic than Sb(V) (Xiong et al. 2020). In recent decades, natural biogeochemical release and anthropogenic activities such as mining, metallurgy, and widespread use of Sb-containing products (e.g., pigments, batteries, and flame retardants) have triggered the Sb contamination in the environment worldwide (Wei et al. 2020; Chen et al. 2022b). Considering the potential teratogenicity and carcinogenicity of Sb to human beings, the World Health Organization (WHO) has set the maximum total Sb limit in drinking water as 20 μg L^{-1} (Zhu et al. 2021). China and Japan have, however, set more stringent limits, which are 5 and 2 μg L^{-1}, respectively (Xiong et al. 2020). Adsorption method using various adsorbents such as activated carbon, carbon nanotubes, and graphene has been found to be an effective and sustainable remediation strategy for the removal of metal(loid)s (Chen et al. 2022c). Nevertheless, high cost of these carbon-based materials has limited the practical potential for their large-scale applications. Therefore, it is of great importance to develop cost-efficient and eco-friendly materials for the removal of Sb anions from aquatic systems, especially for the highly toxic Sb(III) species.

Biochar is a low-cost carbonaceous material produced from the pyrolysis of biomass wastes, with high porosity and abundant surface functional groups (Altaf et al. 2021b; Wu et al. 2021). Biochar has been proven as an excellent adsorbent for the removal of toxic organic compounds (Huang et al. 2018a, b; Qin et al. 2018; Nie et al. 2021), and trace metal(loid)s such as Cd (Chen et al. 2021; Yin et al. 2021), Cr (Wei et al. 2019a; Xu et al. 2020), Pb (Wen et al. 2021; Yang et al. 2021), Hg (Altaf et al. 2021a, b; Liu et al. 2022), As (Pan et al. 2021; Yang et al. 2022), and Sb (Wan et al. 2020; Song et al. 2021; Zhu et al. 2021). Biochar can adsorb metal(loid) ions through multiple mechanisms such as pore filling, ion exchange, precipitation, and surface complexation with functional groups (Hu et al. 2020; Bolan et al. 2022a). To date, due to the limited adsorption/immobilization potential of pristine biochar for pollutants, various modification methods such as magnetization (Zhu et al. 2021), loading of zirconium (Rahman et al. 2021), and chitosan (Palansooriya et al. 2021) have been developed to strengthen biochar's performance in pollutant removal in aquatic systems. The modification processes indeed enhance the adsorption capacity of biochar, yet the extra cost and energy consumption also inevitably rise (Rajapaksha et al. 2016). A prerequisite for the sustainable application of biochar as an effective adsorbent in wastewater treatment is its cost-effectiveness. The adsorption performance of biochar for Sb(III) removal would be closely related to its biomass feedstock source (Cui et al. 2017). Therefore, screening inexpensive and widely sourced feedstock for the preparation of biochar to effectively remove Sb(III) from water is a need of the hour.

Crawfish (*Procambarus clarkii*), distributed worldwide, is one of the common seafood for human (Zhou et al. 2021). China's annual production and export of crawfish in 2018 reached 1.64 million t and 10,801 t, respectively (China Crawfish Industry Development Report 2019). Large-scale consumption of crawfish in the catering industry has rendered the production of a huge volume of crawfish shell bio-waste (Chen et al. 2020b). Approximately, 580,000 t of crawfish shell waste is generated every year in China (Ma et al. 2019). Thus, converting crawfish shells to biochar could be a sustainable solution for the management of this ever-increasing waste resource (Lv et al. 2020). Previous research reported the feasibility of crawfish shell-derived biochar (CSB) for the removal of metal cations including Cd^{2+}, Pb^{2+}, and Cu^{2+} where cation exchange and mineral precipitation appeared as the key adsorption mechanisms (Xiao et al. 2017; Ma et al. 2021; Zhang et al. 2021). The adsorption mechanism of Sb(III) by CSB might differ as compared to metal cations, which remains least understood in the literature. A few studies also reported that biochar could oxidize Sb(III) to Sb(V), decreasing the element's biotoxicity (Wu et al. 2019; Wei et al. 2020; Chen et al. 2022b). However, the oxidation mechanism of Sb(III) on biochar surface through electron transfer reactions, especially those involving persistent free radicals (PFRs), was not thoroughly studied before.

Since pyrolysis temperature can greatly affect the physicochemical characteristics (e.g., abundance of functional groups and electron transfer capacities) of biochar, it can influence biochar's removal efficiency for contaminants (Xiao et al. 2017). Understanding the effect of such characteristics on Sb(III) adsorption/oxidation is crucial for assessing the applicability of CSB for Sb(III) removal from water. This study reports the synthesis of CSB pyrolyzed at 350, 500, and 650°C and its subsequent application to remove Sb(III) from aqueous solutions. The specific objectives of this study were to: (1) determine the adsorption capacity of CSB for Sb(III) under different conditions (i.e., reaction time, initial adsorbate concentration, solution pH, ionic strength, and co-existing substances); (2) unravel the Sb(III) adsorption mechanism using multiple advanced

spectroscopic techniques and theoretical calculations; and (3) elucidate the pyrolysis temperature-depended electron/PFRs mediating mechanisms in the oxidative conversion of Sb(III) to Sb(V) on CSB surface.

2 Materials and methods

2.1 Chemicals and reagents

All the used chemicals in this study were of analytical grade and were purchased from Macklin Bio-Chem Technology Co., Ltd. (Shanghai, China). The chemicals were directly used without further purification. All solutions were prepared with 18.2 MΩ cm^{-1} deionized water (ULPHW-I, Ulupure Co. LTD., China). In addition, the standard solution containing 1000 mg L^{-1} of Sb(III) was obtained from the National Research Center for Certified Reference Materials of China.

2.2 Biochar preparation and characterization

The crawfish shells were collected from a marketplace located in Hangzhou, Zhejiang Province, China. The crawfish shells were rinsed with tap water to remove the impurities, and then oven-dried at 80°C for 24 h prior to biochar production. The CSB was produced by pyrolyzing crawfish shells in a batch pyrolysis furnace at 350, 500, and 650°C under the oxygen-limited condition, with a heating rate of 15°C min^{-1}, and held for 2 h once the final temperature was reached. After pyrolysis, the obtained biochar was labeled as CSB350, CSB500, and CSB650. The biochar was ground, passed through a 100-mesh sieve (0.150 mm), and stored at room temperature for characterization and further experiments. Characterization of selected biochar using multiple spectroscopic techniques including synchrotron-based micro-X-ray fluorescence (μ-XRF) and near-edge X-ray absorption fine structure spectroscopy (NEXAFS) is shown in the Supplementary Material.

2.3 Batch adsorption experiments

A stock solution containing 1000 mg L^{-1} of Sb(III) was prepared by dissolving potassium antimonyl tartrate trihydrate ($C_8H_4K_2O_{12}Sb_2{\cdot}3H_2O$) in deionized water. The working solutions were prepared by the dilution of the stock solution using 0.01 M NaCl solution as the background electrolyte. Batch adsorption experiments were conducted using the methods reported in our previous publication (Chen et al. 2022b). All the adsorption experiments were carried out under dark conditions and replicated three times.

Kinetic adsorption experiments were conducted by adding 0.05 g of biochar (i.e., CSB350, CSB500, and CSB650) into a 25-mL working solution containing 40 mg L^{-1} of Sb(III). The mixture was shaken (180 rpm) for 24 h at 25°C. The initial Sb(III) concentration (40 mg L^{-1}) was based on previous studies (30–50 mg L^{-1}) (Jia et al. 2020; Wei et al. 2020; Chen et al. 2022b). Samples were collected at desired time intervals (5, 10, 15, 30, 60, 120, 240, 360, 480, 600, 720, 960, 1440 min) to determine the residual Sb(III) concentrations in the solution. Adsorption isotherm experiments were conducted by adding 0.05 g of biochar, weighed into a 25-mL working solution with various initial Sb(III) concentrations. The mixture was oscillated at 180 rpm for 24 h at 25°C before the quantitative measurement of residual Sb(III) in the solution. The impact of initial solution pH on adsorption was investigated with a fixed Sb(III) initial concentration (40 mg L^{-1}) at 25°C. The initial solution pH was adjusted in the range of 2–11 using HCl (0.1 M) and/or NaOH (0.1 M) solutions. The influence of ionic strength on Sb(III) adsorption was evaluated with NaCl concentrations varying from 0.01 to 0.25 M, with an initial Sb(III) concentration of 40 mg L^{-1}, at 25°C. Moreover, NO_3^-, Cl^-, SO_4^{2-}, and PO_4^{3-} are ubiquitously found anions in the aqueous system, and thus they were chosen as the model co-existing anions to investigate their influence on Sb(III) removal. The initial concentration of these anions was selected as 40 mg L^{-1}, acting as a typical concentration of anions in wastewater (Wang et al. 2018).

After adsorption, all samples were filtered using a 0.45-μm polyethersulfone (PES) membrane (JINTENG Experimental Equipment. Co., Ltd., China), and the concentration of Sb(III) in the supernatant was quantified using an atomic absorption spectrometer (AAS) (ZA3300, Shimadzu, Japan) equipped with an Sb hollow-cathode lamp (Shanghai Huake Experimental Equipment Co., Ltd., China) at a wavelength of 217.6 nm. The detection limit of Sb concentration was 5 μg L^{-1}. A standard curve within Sb concentration of 0–40 mg L^{-1} was developed using the reference Sb(III) solution. To ensure the accuracy of the data, the spectrometer was recalibrated after measuring each batch of 25 samples, and the relative standard deviation of triplicate analysis was set to < 5%.

The adsorption capacity of biochar and the removal efficiency of Sb(III) were calculated using Eq. [1] and Eq. [2] (Cui et al. 2017):

$$Q_e = (C_o - C_e)V/m \quad \text{(Eq. [1])}$$

$$\eta = (C_o - C_e)/C_o \times 100\% \quad \text{(Eq. [2])}$$

where Q_e (mg g^{-1}) is the adsorption amount at equilibrium; C_o (mg L^{-1}) is the initial concentration of Sb(III); C_e (mg L^{-1}) is the Sb(III) concentration in solution at equilibrium; V (L) represents the solution volume; m (g) is the added mass of biochar; and η (%) is the removal percentage.

2.4 Model fitting for Sb(III) adsorption data

The pseudo-first-order, pseudo-second-order, and intra-particle diffusion models were used to fit the adsorption kinetic data. The Langmuir, Freundlich, and Temkin models were fitted to the adsorption isotherm data. Information of these aforementioned models and their corresponding parameters are presented in the Supplementary Material.

2.5 Desorption and regeneration experiments

Desorption experiments were conducted as follows: the Sb-laden CSB after the batch adsorption experiment was separated through filtration, rinsed with deionized water, and air-dried. The completely dried biochar was added into 25 mL of 0.01 M NaCl solution, oscillated (180 rpm) at 25°C for 24 h (Chen et al. 2022b). Finally, the supernatant was filtered (0.45 μm PES membrane), and the concentration of desorbed Sb was quantified using AAS.

Regeneration of spent CSB was conducted using 0.5 M NaOH solution as a strong desorption agent for 12 h (Wang et al. 2018). The regenerated CSB was thoroughly rinsed with deionized water, air-dried, and added into another fresh Sb(III) solution (40 mg L^{-1}). The adsorption/desorption cycle was repeated four times. The adsorption capacity was calculated at each cycle to assess the reusability of CSB.

2.6 DFT calculations

All the calculations were based on density functional theory (DFT) and performed using Material Studio 8.0 modeling DMol3 package (Delley 1990, 2000). A double numerical quality basis set with polarization functions (DNP) and Perdew-Burke-Ernzerh (PBE) functional basis (Hammer et al. 1999) were used for all calculations. Spin polarization was applied and the real space cutoff radius was maintained at 4.5 Å. Solution effect was considered using the COSMO model, and the solvent was water.

An optimized structure segment containing 55 carbon atoms was generated from a carbon-based monolayer, in which 5 functional groups (–OH, C–O–C, $–CH_3$, C=O, and O=C–O) were assumed. Sb(III) was introduced to the above sites one by one, followed by full relaxation and energy calculation. The bond length was also measured. The adsorption energy (AE) was calculated as follows: AE = E(Sb(III)*)-E(*)-E(Sb(III)), where E(*), E(Sb(III)) and E(Sb(III)*) are the calculated total energies of clean biochar model, free Sb(III) and Sb(III) adsorbed over biochar, respectively. Large negative AE means strong adsorption capacity.

2.7 Statistical analysis

The SPSS 26.0 software was used to perform the statistical analysis. Variability of data was given as the mean ± standard error (n = 3). Significant ($P < 0.05$) difference between treatments was determined using analysis of variance (ANOVA) and Duncan's multiple range t-test. Origin 2021 was employed in the data graphing.

3 Results and discussion

3.1 Characteristics of biochar

Selected physicochemical characteristics of CSB are presented in Table 1. From CSB350 to CSB650, the decrease of C, H and O contents in CSB was mainly attributable to the loss of volatile C-containing components (Ma et al. 2021), and the destruction of N/H-containing compounds (Wei et al. 2019b). The higher pH and surface alkalinity (SA) of biochar, pyrolyzed at higher pyrolysis temperature (650°C), were due to the destruction of acidic functional groups (e.g., phenolic and carboxylic) (Sun et al. 2021), and/or the formation and accumulation of alkaline mineral substances (e.g., carbonates) (Chen et al. 2020a). The increase in cumulative alkaline elements (e.g., K, Na, Ca, and Mg) with increasing pyrolysis temperature simultaneously caused a higher ash content in biochar (Wei et al. 2019b). The enhancement of biochar surface area and pore volume to increased pyrolysis temperature was due to the decomposition of carbohydrates, and thus enhanced the formation of micropores and/or exposure of the inner surface (Sun et al. 2021; Altaf et al.

Table 1 Selected physicochemical characteristics of crawfish shell biochar pyrolyzed at 350°C, 500°C and 650°C

Sample [a]	C (%)	H	N	S	pH (H_2O)	Ash content (%)	Surface alkalinity (cmol kg^{-1})	Specific surface area (m^2 g^{-1})	Pore volume (cm^3 g^{-1})
CSB350	47.9	5.0	3.5	0.03	8.5	27.0	271	3.2	0.004
CSB500	27.4	1.0	2.3	0.02	9.2	38.6	288	4.4	0.031
CSB650	25.5	0.5	1.6	0.02	10.6	47.3	303	12.1	0.054

[a] CSB350, CSB500, and CSB650 indicate the crawfish shell biochar pyrolyzed at 350°C, 500°C, and 650°C, respectively

2022). Metal concentrations in the CSB showed a gradual increase with increasing pyrolysis temperature (Table S1), which was probably attributable to the volatilization losses of major elements such as C, H, and N, thereby concentrating the metallic elements (Xiao et al. 2017). The low content of heavy metals indicated that the CSB holds the potential to be applied as environmentally-friendly adsorbent.

The SEM images exhibited a denser morphology and stunted porosity of CSB350 compared to other biochars (Fig. 1). An increasing pyrolysis temperature endowed the biochar with more developed pore channels, exhibiting a fiber-like honeycomb structure (Fig. 1). These results confirmed higher surface area and pore volume in CSB650 than other two biochars (Table 1). Results of TEM analysis indicated a rough surface morphology with discernible particles on CSB surfaces (Fig. 1), suggesting the probable presence of mineral substances such as calcium carbonate. The XRD patterns confirmed that the mineral crystals in CSB were mainly $CaCO_3$, and a small amount of NaCl (Fig. S1) inherited from the feedstock material. The EDS spectra of CSB confirmed that higher pyrolysis temperature enhanced the contents of alkaline metals such as Na, K, Mg and Ca in biochar (Fig. S2). As demonstrated in the TGA and DGT patterns of CSB (Fig. S3), 43%, 59%, and 60% of weight losses were noted in the case of CSB350, CSB500, and CSB650, respectively. The decomposition of CSB350 started at about 300°C with two maximum weight losses peaked at 457°C and 713°C, and the temperature of sharp mass decay was found to be at 737°C for CSB500 and 753°C for CSB650 (Fig. S3B). The first mass loss for CSB350 at 457°C represented the likely decomposition of calcium hydroxide (Habte et al. 2020). On the other hand, the weight loss of CSB above 700°C was due to the thermal destruction of the mineral contents of biochar (Park et al. 2018), i.e., calcite ($CaCO_3$) identified by XRD in this study (Fig. S1).

As shown in Fig. S4, CSB350 exhibited an advantage in the diversity of surface functional groups over the other two biochars, including O–H stretching vibrations of alcoholic hydroxyl group (3410 cm^{-1}) (Wei et al. 2020), stretching vibrations of C–H bonds (–CH– at 2922 cm^{-1} and $–CH_2–$ at 2850 cm^{-1}), carbonyl C = O (1580 cm^{-1}) (Chen et al. 2022a), O–C = O of the carbonates (1410 cm^{-1}) (Ma et al. 2021), aromatic ether C–O–C bonds (1040 cm^{-1}), and vibrations of aromatic C–H out-of-plane groups (875 and 713 cm^{-1}) (Xu et al. 2020). This phenomenon suggested that CSB350 might hold the potential to adsorb Sb(III) via chemisorption process. As for the CSB500 and CSB650, the stretching vibrations of O–H bond, C–H bond, and C = O disappeared, whereas enhanced bands for O–C = O, aromatic ether C–O–C, and aromatic C–H bonds were observed (Fig. S4). The high temperature-induced degeneration of O–H vibration peak was attributable to the decomposition of the hydroxyl

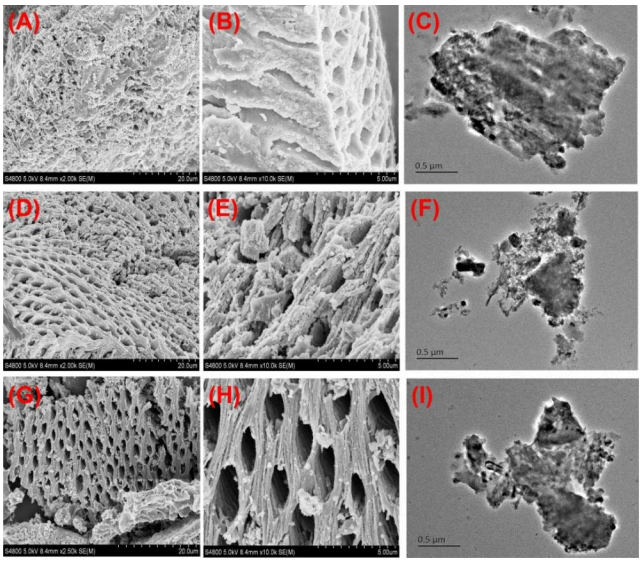

Fig. 1 Scanning electron microscope (SEM) images of CSB350 (A and B), CSB500 (D and E) and CSB650 (G and H); and the transmission electron microscope (TEM) images of CSB350 (C), CSB500 (F) and CSB650 (I). CSB350, CSB500, and CSB650 indicate the crawfish shell biochars pyrolyzed at 350 °C, 500 °C, and 650 °C, respectively

groups bonded by hydrogen and oxygen bonds (Park et al. 2018). The disappearance of C–H and C = O peaks was caused by the transformation of O-alkylate groups to volatile or fixed carbon (e.g., C–O, C–O–C) with the increase in pyrolysis temperature (Xu et al. 2020; Ma et al. 2021). Enhanced peaks centered at 875 and 731 cm^{-1} indicated the promotion of "biochar's" aromaticity under high-temperature pyrolysis (Cui et al. 2017). In addition, the peaks observed around 605 and 567 cm^{-1} in CSB were associated with O–P–O bonds (Park et al. 2018).

The XPS spectra verified that the increasing pyrolysis temperature led to higher proportions of O 1s, Ca 2p, N 1s, and Na 1s in biochar, and a lower C 1s peak proportion (Fig. S5). The C 1s spectra (Fig. 2 A) of CSB350 could be deconvoluted into three peaks, i.e., 284.8, 285.2, and 288.9 eV, which were assigned to the C–C (50.0%), C = C (42.6%), and HO–C = O groups (7.4%), respectively (Zeng et al. 2019; Palansooriya et al. 2021). For O 1s, CSB350 displayed two peaks at 531.6 and 532.4 eV (Fig. 2D), which represented C–O and C = O, respectively (Liu et al. 2019). As the pyrolysis temperature increased, C = C peak in CSB350 disappeared, whereas HO–C = O peak proportion increased from 7.4% in CSB350 to 12.8% in CSB500, and 18.7% in CSB650 (Fig. 2 A-C). A new C–O–C peak in CSB500/650 was observed, and its peak intensity positively responded to the increasing pyrolysis temperature (Fig. 2B, C), which was consistent with the results in FTIR spectra (Fig. S4). The peak intensity and location shift in C 1s and O 1s of CSB indicated that the pyrolysis temperature was

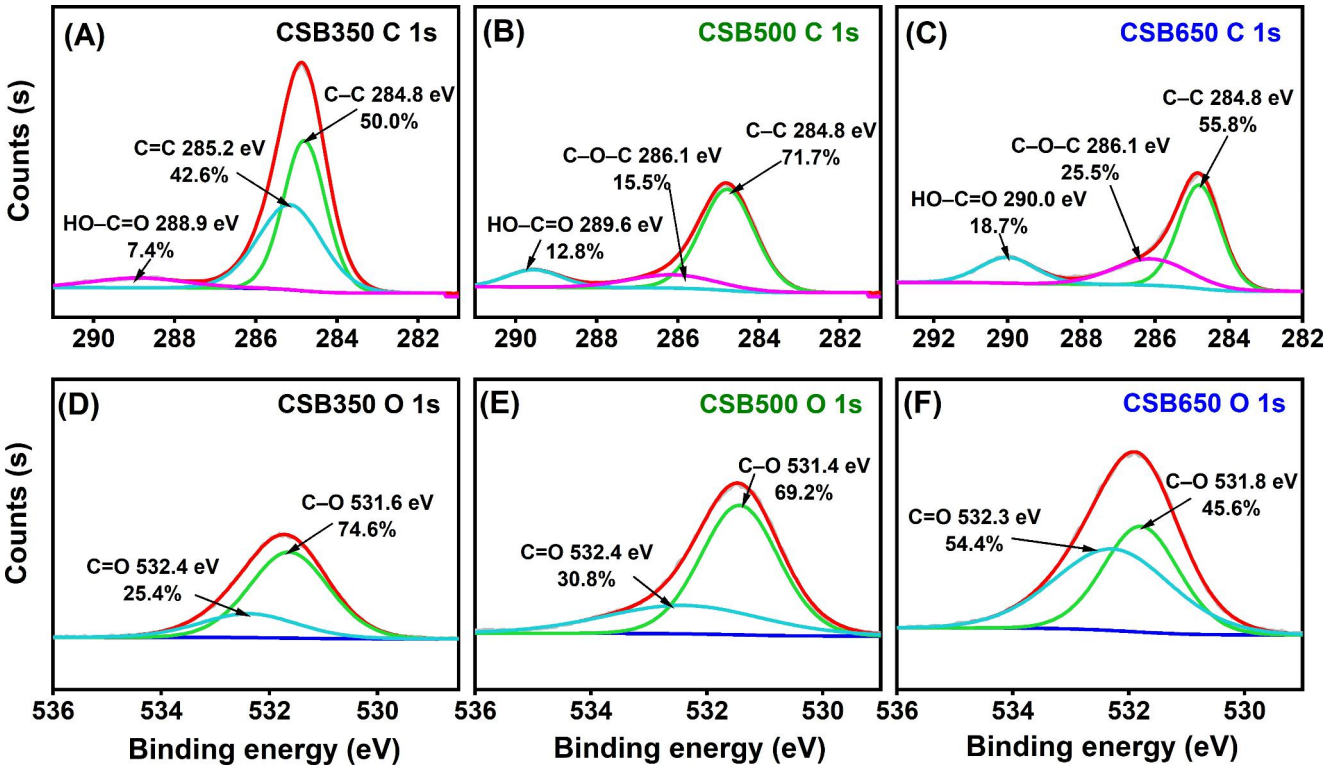

Fig. 2 XPS spectra of C 1s (A, B, C) and O 1s (D, E, F) for crawfish shell biochar (CSB) pyrolyzed at 350°C (CSB350), 500°C (CSB500), and 650°C (CSB650) before adsorption

a key factor influencing the diversity and composition of functional groups.

3.2 Sb(III) adsorption and desorption

3.2.1 Adsorption kinetics

Kinetic data revealed that the adsorption of Sb(III) by CSB increased rapidly in the first 30 min, accounting for 92–96% of the total adsorption; then the adsorption rate gradually slowed down until equilibrium reached (Fig. 3 A). The kinetic adsorption data for Sb(III) were fitted to the pseudo-first-order, pseudo-second-order (Fig. 3 A), and intra-particle diffusion models (Fig. 3B), and the associated fitting parameters are presented in Table S2. The pseudo-second-order model best described the kinetic data with the highest R^2 values (0.84–0.97) (Table S2). The theoretically calculated Q_e value also agreed closely with the obtained experimental data, indicating that chemical interactions occurred between functional groups on the biochar surface and Sb(III) anions (Xiong et al. 2020).

The intra-particle diffusion model fitting results suggested that more than one rate-limiting steps were involved during the Sb(III) adsorption process, as the curve of Q_t versus $t^{0.5}$ was multi-linear with an intercept of $C \neq 0$ (Fig. 3B; Table S2), as indicated by Rusmin et al. (2015). The Sb(III) adsorption process could be divided into two linear stages. At the first fast-stage (0–60 min), the higher K_1 value represented the high adsorption rate, implying the rapid occupancy of Sb(III) on the available active sites, which was mainly due to the film diffusion where Sb(III) was diffused towards the surface of biochar (Rusmin et al. 2015; Xiong et al. 2020). As the majority of adsorption sites were occupied by Sb(III), the adsorption process entered the second slow stage (60-1440 min), i.e., an intra-particle diffusion governed Sb(III) adsorption into the internal pores of biochar (Liu et al. 2019).

3.2.2 Adsorption isotherm

The Langmuir, Freundlich, and Temkin models were fitted to the adsorption isotherm data of Sb(III) (Fig. 3 C), and their corresponding parameters are listed in Table S3. As compared to the Freundlich fitting results, the Langmuir model provided higher R^2 values ranging from 0.97 to 0.99, indicating that Sb(III) adsorption was much closer to a monolayer adsorption, rather than a multilayer adsorption (Chen et al. 2022b). As predicted from the Langmuir model, the maximum adsorption capacity (Q_m) was found to be 27.7, 18.2, and 16.1 mg g^{-1} for CSB350, CSB500, and CSB650, respectively (Table S3), indicating that the increase of pyrolysis temperature negatively affected the removal of

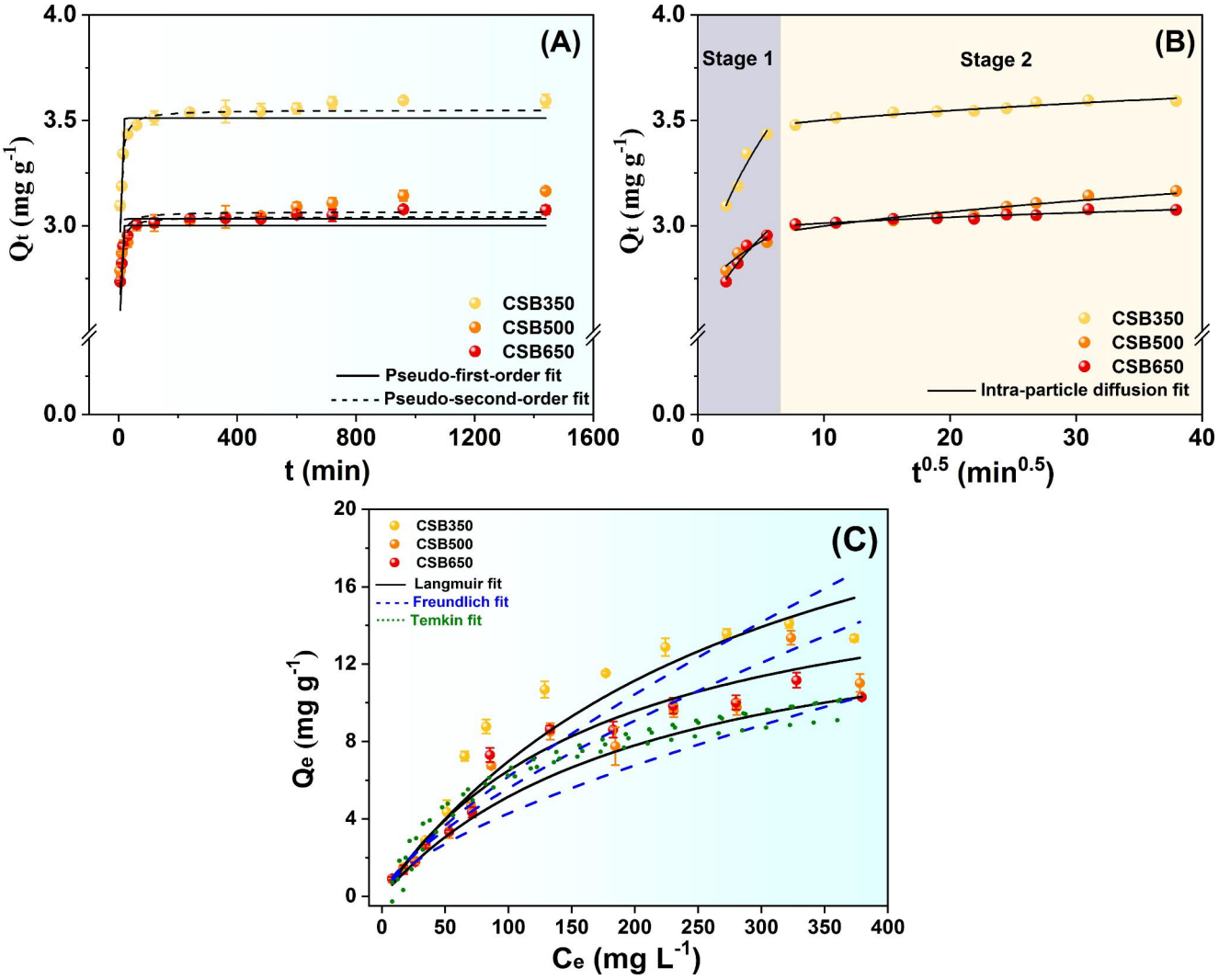

Fig. 3 Adsorption kinetics of Sb(III) on crawfish shell biochar (CSB) pyrolyzed at 350°C (CSB350), 500°C (CSB500), and 650°C (CSB650) using pseudo-first-order, pseudo-second-order (A), and Intra-particle diffusion models (B); adsorption isotherms of Sb(III) on the CSB (C)

Sb(III) by biochar. The Sb(III) adsorption isotherm did not fit well by the Temkin model ($0.72 < R^2 < 0.99$), suggesting that the adsorption process might not be greatly affected by the adsorbate/adsorbate interactions (Chen et al. 2022b).

The adsorption capacities of other carbon-based adsorbents and CSB350 for Sb(III) were compared and are summarized in Supplementary Material (Table S4). It shows that CSB350 has a considerably higher Sb(III) adsorption capacity than some pristine biochars, reported in literature (e.g., Vithanage et al. 2015; Cui et al. 2017; Han et al. 2017; Jia et al. 2020; Ji et al. 2022), activated carbon (Yu et al. 2014), carbon nanotubes (Salam and Mohamed 2013), and graphene-based adsorbents (e.g., Yang et al. 2017; Capra et al. 2018). The CSB350 exhibits high Sb(III) adsorption capacity in addition to its low-cost advantage, rendering it a potentially feasible adsorbent for Sb-contaminated water remediation. In addition, CSB350 is also a good precursor if we select biochar for modification to obtain greater removal of Sb(III).

3.2.3 Influence of ionic strength and co-existing substances on Sb(III) adsorption

The adsorption of Sb(III) onto CSB was insignificantly ($P > 0.05$) affected by the solution ionic strength ranging from 0.01 to 0.2 M (Fig. 4 A). This phenomenon indicated inner-sphere complex formation between Sb(III) and functional groups on biochar surface (Rahman et al. 2021). The high ionic strength (0.25 M) suppressed the adsorption capacity of CSB350, CSB500, and CSB650, and adsorption was found to decrease by 15%, 14%, and 11%, respectively, as compared to the 0.01 M treatment (Fig. 4 A). The elevated degree of charge screening caused by increased Na^+

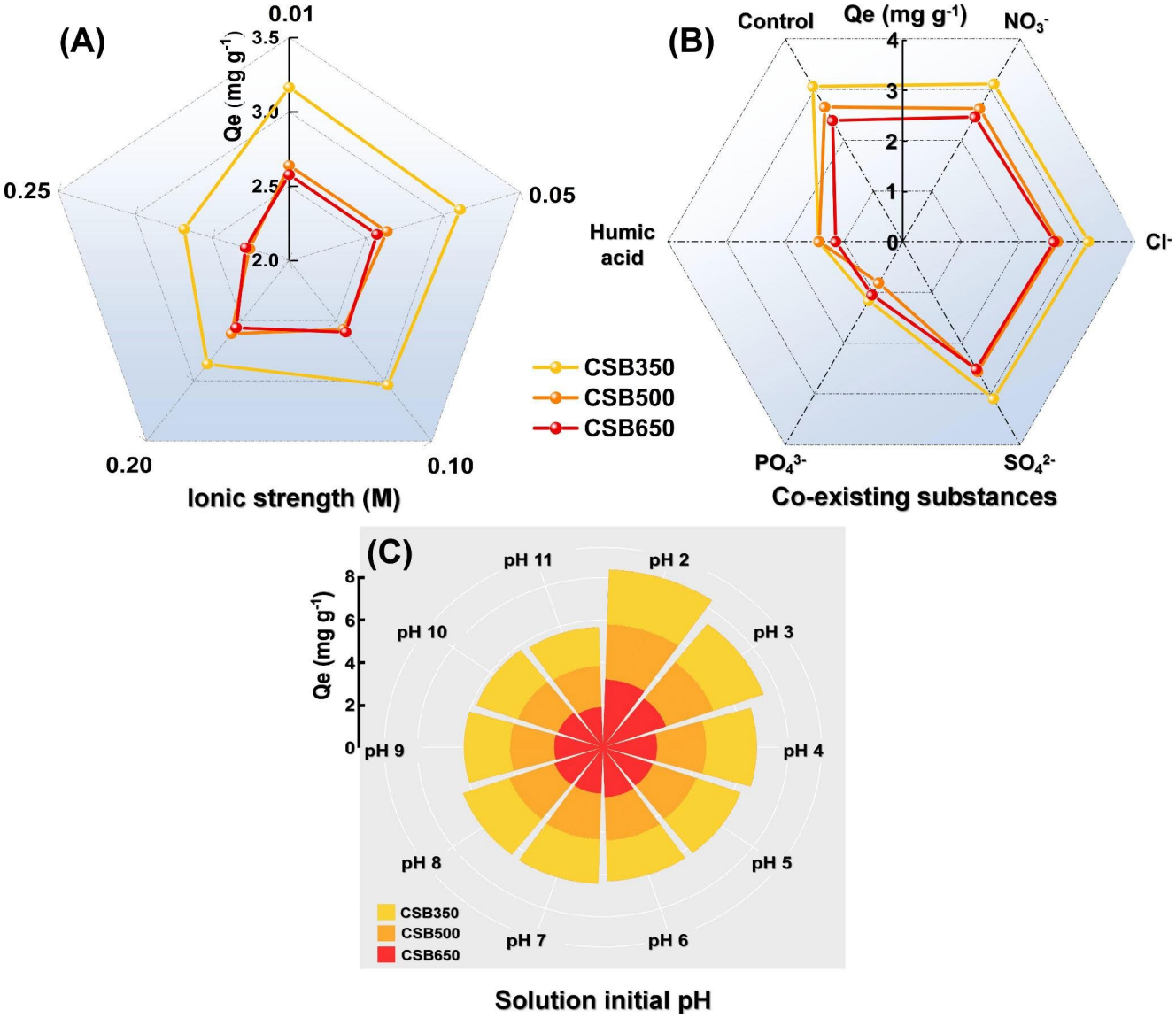

Fig. 4 Effects of ionic strength (A), co-existing substances (B), and initial solution pH (C) on Sb(III) adsorption by crawfish shell biochar (CSB) pyrolyzed at 350°C (CSB350), 500°C (CSB500), and 650°C (CSB650)

ions might be responsible for the decreased Sb(III) removal at high ionic strength, as suggested by Chen et al. (2022b).

As illustrated in Fig. 4B, the presence of NO_3^-, Cl^-, and SO_4^{2-} showed an insignificant ($P > 0.05$) influence on Sb(III) adsorption by CSB, which was in agreement with the conclusion by Wan et al. (2020). However, the co-existing PO_4^{3-} significantly ($P < 0.05$) suppressed Sb(III) adsorption on CSB, with a decrease of 56–69% (Fig. 4B). The anion PO_4^{3-} has a similar molecular structure to antimonite (Wang et al. 2018), and they may compete for the same active adsorption sites. Park et al. (2018) reported that CSB showed a strong affinity to phosphate. Therefore, the presence of PO_4^{3-} could significantly impede the Sb(III) adsorption performance of CSB via competitive adsorption (Xi et al. 2013). Moreover, the introduced humic acid (HA) significantly ($P < 0.05$) inhibited the adsorption of Sb(III) on CSB by 46.4–52.3%, as compared to the control (Fig. 4B). This could be attributable to the blockage of surface reactive sites on biochar by the large-molecular HA (Wei et al. 2020).

3.2.4 Influence of initial solution pH on Sb(III) adsorption

The highest adsorption of Sb(III) on CSB350 was noted at pH 2, up to 3.2 mg g^{-1} (Fig. 4 C). The response of Sb(III) adsorption to the initial solution pH might be due to changes in speciation of Sb(III) at different pH conditions (Xiong et al. 2020). Under strongly acidic conditions at pH of 2,

the dominating species of Sb(III) would be electropositive $Sb(OH)_2^+$, and electrostatic interaction might occur between the electronegative surface of CSB and electropositive $Sb(OH)_2^+$, thus promoting Sb(III) adsorption (Wan et al. 2020). When the initial solution pH ranged from 3 to 6, the amount of $Sb(OH)_2^+$ decreased, which suppressed the electrostatic interaction between biochar and $Sb(OH)_2^+$, thus decreasing Sb(III) adsorption (Cui et al. 2017). To be specific, at initial solution pH of 6, the adsorption of Sb(III) on CSB350, CSB500 and CSB650 decreased by 30.5%, 21.7%, and 21.8%, respectively, as compared to the adsorption at pH 2 (Fig. 4 C). At a pH range of 6 to 11, Sb(III) adsorption on CSB appeared not to be affected significantly by the solution pH, as the adsorption amount of Sb(III) only slightly varied. These results could be explained by the fact that the predominant form of Sb(III) was $Sb(OH)_3^0$ at this specific pH range, which was not readily adsorbed by biochar due to its electroneutrality (Xiong et al. 2020).

3.2.5 Desorption and regeneration of biochar

As expected, desorption of Sb(III) from CSB350, CSB500, and CSB650 increased with the increase of desorption time, and the desorption process tended to be stable after 4 h (Fig. S6A). After 24 h of desorption, CSB350 retained 88% of the maximum adsorption capacity of Sb(III), slightly lower than that of CSB500 (90%) and CSB650 (90%). The desorption results indicated a robust resistance of CSB to desorb Sb(III) anions. Moreover, the Sb-adsorbed CSB350 was desorbed using NaOH solution (0.5 M) to test its reusability. The regeneration results demonstrated that Sb(III) adsorption efficiency of CSB350 was maintained 83.1% of the maximum adsorption capacity after 3 adsorption-desorption cycles (Fig. S6B), suggesting that CSB held potential reusability in practical application.

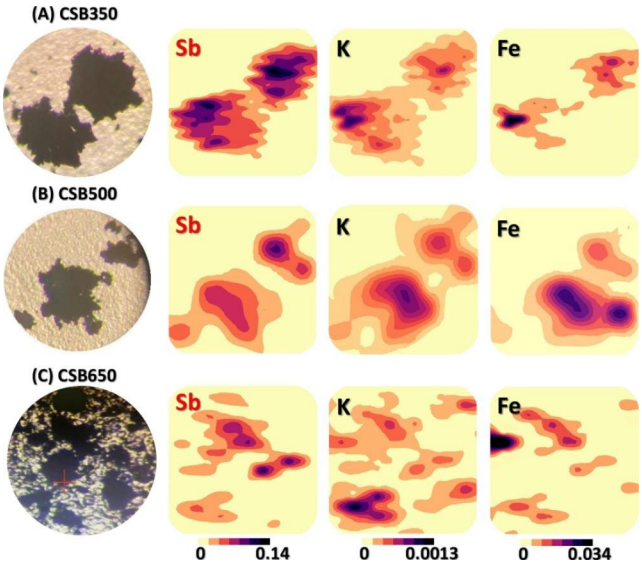

Fig. 5 The microscope photos and μ-XRF maps of Sb, K, and Fe distribution within Sb-laden CSB350, CSB500, and CSB650 particles. CSB350, CSB500, and CSB650 indicate the crawfish shell biochar pyrolyzed at 350°C, 500°C, and 650°C, respectively. Higher fluorescence intensities indicate higher concentrations of elements

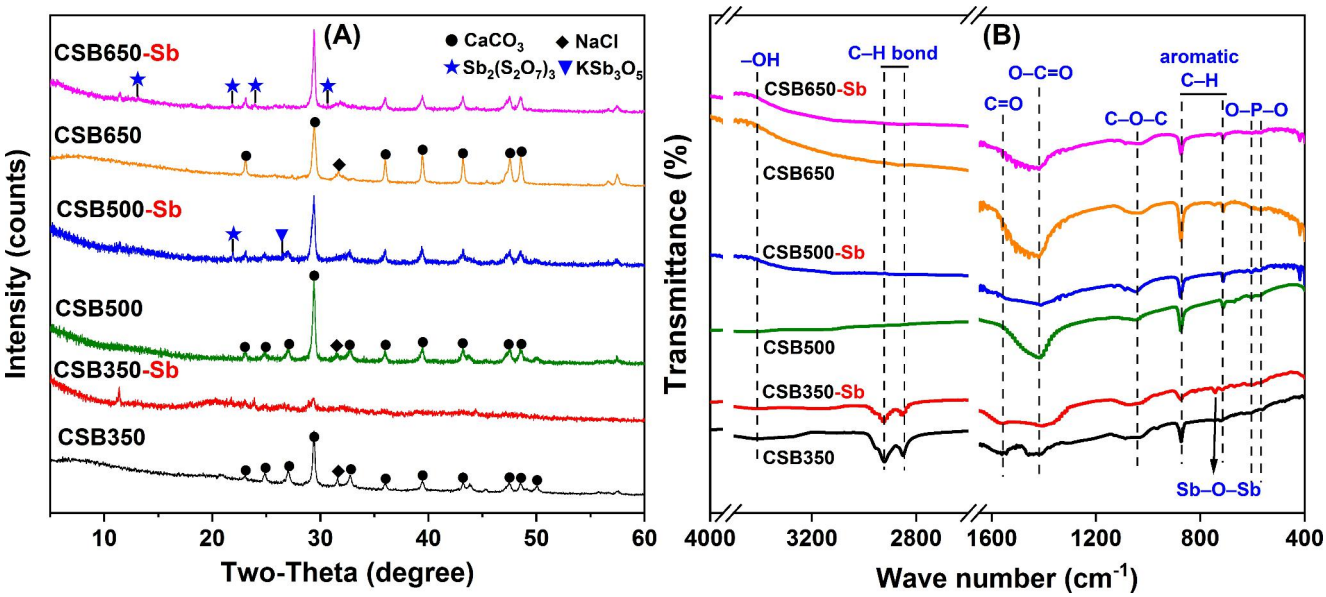

Fig. 6 X-ray diffraction (XRD) patterns (A) and FTIR spectra (B) of crawfish shell biochar (CSB) pyrolyzed at 350°C (CSB350), 500°C (CSB500), and 650°C (CSB650) before and after Sb(III) adsorption

3.3 Qualitative analysis on biochar surface after Sb(III) adsorption

The μ-XRF-based elemental mapping of CSB after Sb(III) adsorption confirmed the presence of Sb and mineral elements (i.e., K and Fe) on the biochar surface, with a heterogeneous distribution (Fig. 5). The greater density and brightness of Sb dots were observed in the Sb-laden CSB350 (Fig. 5 A), indicating its higher adsorption capacity than CSB500 and CSB650. Additionally, the Sb distribution area was not consistent with that of Fe distribution area, which might suggest that the Fe-Sb complex formation was not a key Sb(III) adsorption mechanism in this study. The HR-TEM based elemental mapping revealed the distribution change of non-metal elements (i.e., C, O, N, P) in biochar (Fig. S7). The weakened intensities for C and O might indicate the contribution of C/O-containing groups in the Sb(III) adsorption process. The CSB350 containing more C and O groups showed higher Sb(III) adsorption than CSB650, confirming the μ-XRF and HR-TEM results.

Furthermore, the presence of crystallographic phase of Sb on the biochar surface was investigated using XRD analysis (Fig. 6 A). In addition to the diffraction reflection of calcium carbonate, several new reflections occurred in the Sb-laden CSB. For instance, based on the Powder Diffraction File (PDF) database, antimony sulfate $Sb_2(S_2O_7)_3$ (Card #34-1097) was detected in Sb-laden CSB650, while potassium antimony oxide (KSb_3O_5) (Card #31–0973) and $Sb_2(S_2O_7)_3$ were simultaneously observed in Sb-laden CSB500 (Fig. 6 A). Although CSB350 exhibited the highest

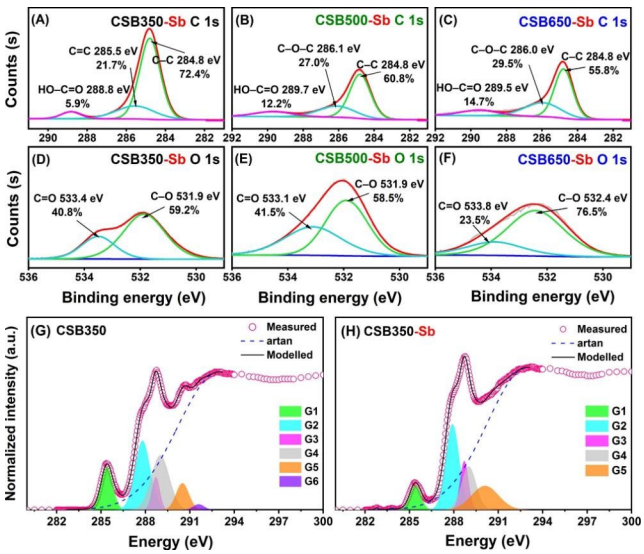

Fig. 7 XPS spectra of C 1s (A, B, C) and O 1s (D, E, F) for crawfish shell biochar (CSB) pyrolyzed at 350°C (CSB350), 500°C (CSB500), and 650°C (CSB650) after Sb(III) adsorption; Carbon K-edge NEXAFS spectra of CSB350 (G) and Sb-laden CSB350 (H). G1-G6 represent six Gaussian curves and Artan represents an arctangent step function. All deconvolution results are listed in Table S5

Sb(III) adsorption, the Sb-laden CSB350 showed no Sb-related crystal phases, indicating the presence of Sb on CSB350 surface as an amorphous phase. This could be ascribed to the low mineral content in CSB350, as revealed by the EDS spectra (Fig. S2), which confined the formation of antimony crystal phases on this adsorbent.

3.4 Potential adsorption mechanisms

3.4.1 FTIR, XPS and NEXAFS analyses

Noticeable changes of FTIR band features occurred in CSB after interaction with Sb(III) (Fig. 6B). The CSB350 sample was used as a reference to study the role of surface functional groups of biochar in Sb(III) adsorption. Firstly, the band for O–H groups disappeared (Fig. 6B), highlighting the role of hydrogen bonding in Sb(III) adsorption. The hydroxyl groups could serve as hydrogen donors to bond with oxygen atoms from Sb(III), as suggested by Xiong et al. (2020). Secondly, a weakened intensity of aromatic C–H out-of-plane vibrations was noted (Fig. 6B), indicating that the Sb(III)-π interaction occurred during Sb(III) adsorption (Cui et al. 2017). A stable combination of a π from aromatic C–H with another π from Sb(III) anions could enhance the adsorption onto biochar (Xiong et al. 2020). Thirdly, the stretching vibrations of oxygen-containing groups such as C = O and C–O were also weakened with slight shift in peak position (Fig. 6B). These results suggested that the oxygen-containing functional groups on biochar also participated in Sb(III) adsorption via surface complexation reaction (Jia et al. 2020). Instead, a new band centered at 743 cm^{-1} was noted, which could be assigned to the stretching vibrations of Sb–O–Sb (Wei et al. 2020), as also demonstrated by XPS data, confirming the presence of Sb(III) on the biochar surface.

High-resolution XPS spectra of C 1s and O 1s for Sb-laden CSB are shown in Fig. 7 A-F. The C 1s spectra of CSB350 illustrated that C = C peak proportion decreased from 42.6 to 21.7% after Sb(III) adsorption (Fig. 7 A), implying a π–π coordination between aromatic C = C bonds and Sb(III) anion (Chen et al. 2022b). As for the C 1s spectra of CSB500, the ratio of C–C peak decreased from 71.7 to 60.8% after Sb(III) adsorption (Fig. 7B). In addition, in the Sb-laden CSB650, the carboxyl peak in C 1s spectra shifted from 290.0 to 289.5 eV (Fig. 7 C), with a proportional decrease of 4%. The proportion change and peak shift of carboxyl stressed the key factor of surface complexation during CSB650-Sb(III) interaction. In the O 1s spectra of the three CSB, Sb adsorption had a noticeable impact on the peak shift and proportion change of C–O and C = O groups, to positions with higher binding energy (Fig. 7D-F). This indicates the contribution of oxygen-containing

groups during the adsorption process, such as the formation of C–O–Sb bonds (Chen et al. 2022b). For instance, in the O 1s spectra of CSB350, a decrease of peak proportion for C–O from 74.6 to 59.2% occurred, which highlighted its crucial role in Sb(III) adsorption on the biochar (Fig. 7 F).

The NEXAFS-based C 1s spectroscopic analysis was employed to further identify the C species of CSB350 before and after Sb adsorption (Fig. 7G, H). The assignment of C 1s deconvolved peaks was obtained from previous publications (Wei et al. 2019a; Li et al. 2020). The C 1s NEXAFS spectra illustrated that alkyl C (G1, 32.6%), O-alkyl C (G4, 30.8%), carbonyl-related C (G3 + G5, 18.7%), and aromatic C (G1 + G6, 17.1%) were the dominant C species on CSB350 (Table S5). After interaction with Sb, the proportion of aromatic C = C decreased from 15.3 to 8.3%, and the peak for aromatic C–C disappeared (Fig. 7 H; Table S5). Concomitantly, Sb association resulted in a pronounced decrease in the O-alkyl C peak, from 30.8 to 20.5% (Table S5). These feature changes strongly suggested the interaction of Sb ions with aromatic C = C/C–C and C–OH groups on the CSB350 surface, which coincided with the results of FTIR and XPS analyses.

3.4.2 DFT calculations

The Sb(III) adsorption capacities of CSB at different reaction sites were verified using DFT calculations. The optimized structure segment of CSB with 5 functional groups (–OH, C–O–C, $–CH_3$, C = O, and O = C–O) is presented in Fig. 8 A. As demonstrated in Fig. 8B-F, the calculated adsorption energy (AE) values of O = C–O (-2.94 eV) and C = O (-1.81 eV) were remarkably higher than those of –OH (-0.49 eV), C–O–C (-0.10 eV) and $–CH_3$ (-0.04 eV). Additionally, O–Sb bond distances in various reaction sites were obtained, showing the order C = O (2.00 Å) < O = C–O (2.16 Å) < –OH (2.35 Å) < $–CH_3$ (2.78 Å) < C–O–C (3.64 Å). Active sites with large negative AE and short bond length were identified as promising features for Sb(III) adsorption on biochar (Zhang et al. 2019a; Chen et al. 2022b). These results further confirmed the strong Sb(III) adsorption capacity of O = C–O and C = O groups, highlighting that surface complexation was the key adsorption mechanism in the removal of Sb(III) by CSB. The DFT studies also suggested that hydrogen bonding and π–π coordination, respectively, triggered by hydroxyl and aromatic methyl might play a secondary role in the Sb(III) adsorption due to the low calculated AE (Fig. 8B, D).

Overall, FTIR, XPS, and NEXAFS analyses and theoretical calculations confirmed the key role of functional groups in the Sb(III) adsorption process. CSB350 with abundant surface functional groups such as C = O, O = C–O, hydroxyl, and aromatic C–H has shown the greatest adsorption capacity for Sb(III). Therefore, it is recommended as the most suitable sorbent in the removal of aqueous Sb(III).

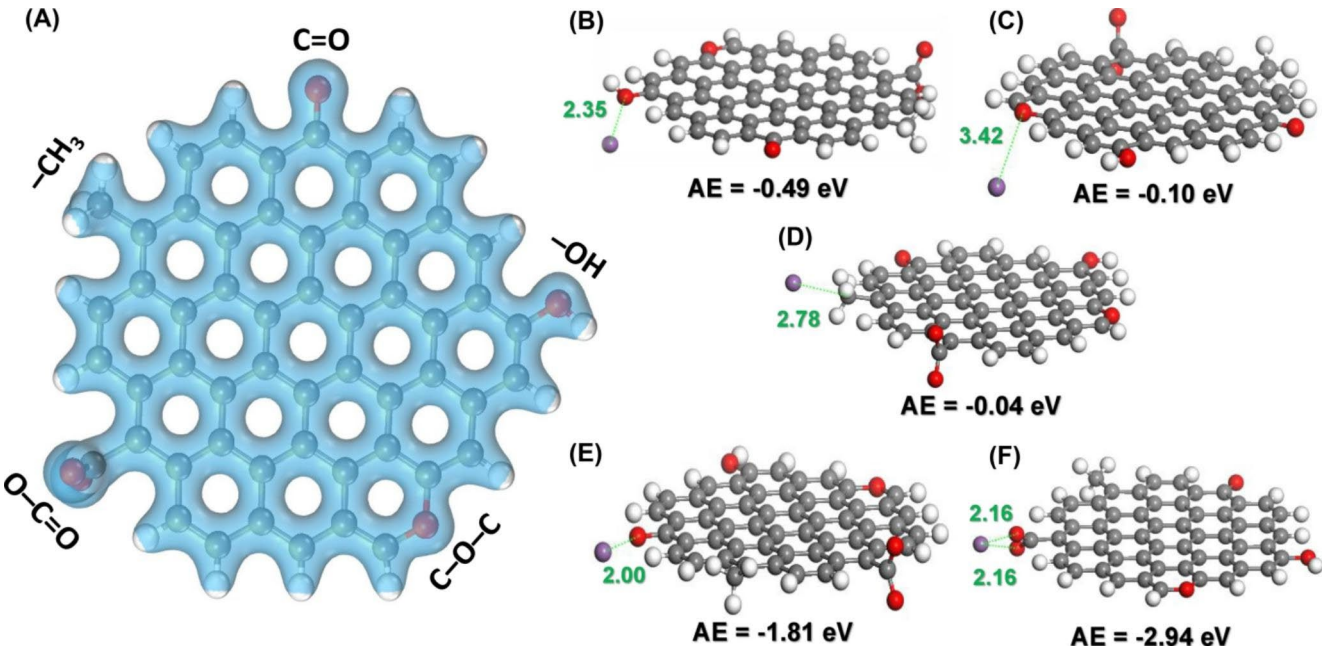

Fig. 8 DFT calculations of Sb(III) adsorption. Basic framework of carbon substrate with five functional groups (–OH, C–O–C, $–CH_3$, C = O and O = C–O) (A); and fully optimized geometries and adsorption energy (AE) with Sb(III) adsorbed by –OH (B); C–O–C (C); $–CH_3$ (D), C = O (E), and O = C–O (F). Sb, C, O and H are shown as purple, grey, red and white balls, respectively. Electron density is shown with transparent blue isosurface in (A) with an isovalue of 0.5 e/Å^3. Sb-O distance (green lines) in (B)-(F) is labelled in unit of Å

3.5 Oxidation of Sb(III) on biochar surface

The oxidation state of Sb was examined following Sb(III) adsorption on biochar by the deconvolution of Sb 3d photoelectron spectra. Given the narrow scan of Sb $3d_{5/2}$ overlapping with the O 1s region, the Sb $3d_{3/2}$ spectra were applied to determine the oxidation state of Sb on CSB, and the deconvolution results are shown in Fig. 9 A. As demonstrated, Sb(V) proportion in the CSB decreased in the order of CSB350 (78%) > CSB650 (61%) > CSB500 (45%). It was reported that Sb(III) oxidation by O_2 in the nature is a slow process (Cui et al. 2017; Wei et al. 2020). Hence, the oxidation phenomenon was most likely influenced by the biochar addition.

Biochar-derived persistent free radicals (PFRs) may favor the oxidation of Sb(III) (Wei et al. 2020). Electron spin resonance (ESR) analysis was employed to identify the presence of PFRs on selected biochar samples. All three CSBs generated pronounced ESR signals, and the concentration of PFRs decreased in the following order: CSB500 > CSB350 > CSB650 (Fig. 9B-1). The intensity of ESR signal increased from CSB350 to CSB500, suggesting that the increasing pyrolysis temperature favored the formation of PFRs in biochar (Cui et al. 2017). The decrease of ESR signals in CSB650 could be ascribed to the destruction and reorganization of some organic structures in the biochar (Yang et al. 2016). Moreover, the ESR signal decreased after Sb(III) adsorption by CSB350 (Fig. 9B-2), suggesting the involvement of PFRs in biochar during the biochar-Sb interaction process. Therefore, an ESR analysis using DMPO (a typical spin trapping agent) was employed to identify the specific free radical species. Results showed that DMPO-•OH and DMPO-$•O_2^-$ were detected as the major active free radical species, and the intensity of •OH signal was higher than that of $•O_2^-$ (Fig. S8). Therefore, the oxidation of Sb(III) might be induced by CSB-derived PFRs, i.e., •OH was the major oxidative radical species whilst $•O_2^-$ also contributed to the oxidation process (Huang et al. 2018a, b; Li et al. 2019). However, the oxidation capacities of CSBs (CSB350 > CSB650 > CSB500) were not in accordance with their corresponding concentration of PFRs (CSB500 > CSB350 > CSB650). This phenomenon indicated that Sb(III) oxidation by biochar was not solely governed by PFRs.

It was thus hypothesized that Sb(III) oxidation could also be affected by the electron transfer property of biochar, i.e., the electron-donating capacity (EDC) and electron-accepting capacity (EAC). The values of EDC and EAC were calculated (Fig. S9) and are presented in Fig. 10 A. As the pyrolysis temperature increased, CSB displayed decreasing EDC from 0.128 to 0.085 mmol e^- (g biochar)$^{-1}$, while the EAC increased from 0.055 to 0.130 e^- (g biochar)$^{-1}$. The electron exchange capacity (EEC) was obtained by summing up EAC and EDC. An increasing pyrolysis temperature caused a decrease of EDC/EEC and an increase of EAC/EEC (Fig. 10B), indicating that CSB350 possessed the strongest reducing capacity and CSB650 had the highest oxidizing capacity (Klüpfel et al. 2014; Zhang et al. 2019b;

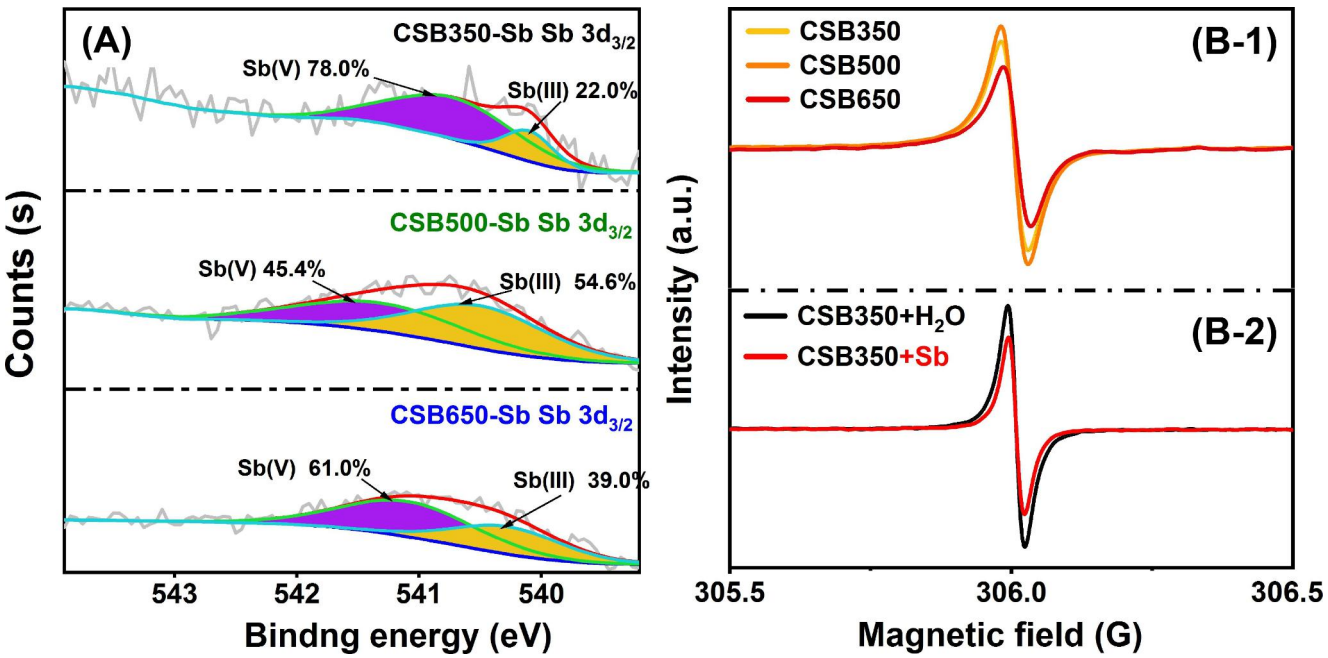

Fig. 9 The Sb $3d_{3/2}$ XPS spectra of Sb-adsorbed crawfish shell biochar (CSB) pyrolyzed at 350°C (CSB350), 500°C (CSB500), and 650°C (CSB650); ESR spectra of CSB before adsorption (B-1); CSB350 in the blank solution and after adsorption of Sb(III) (B-2)

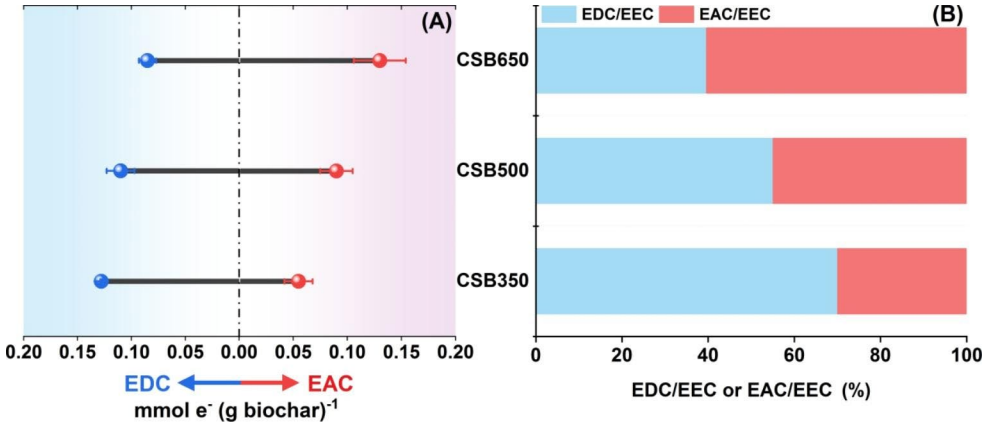

Fig. 10 Electron donating capacities (EDCs), electron accepting capacities (EACs) (A) of crawfish shell biochar (CSB) pyrolyzed at 350°C (CSB350), 500°C (CSB500), and 650°C (CSB650); the relative proportions of EAC and EDC values to the total electron exchange capacities (EEC, EEC = EDC + EAC) (B). The EAC and EDC values are presented as the average ± standard deviation from triplicate analyses. The corresponding oxidative/reductive current responses to increasing amounts of biochar using mediated electrochemical analyses are provided in the Supplementary Material (Fig. S9)

Cui et al. 2017) reported that the electron-donating phenolic moieties in biochar firstly might have reduced solution-derived molecular oxygen to reactive oxygen species (ROS, $\bullet O_2^-$), then the generated ROS facilitated the Sb(III) oxidation in aqueous solution, and finally Sb(V) was adsorbed on the biochar surface. We infer that the high EDC of CSB350 was the most plausible reason for its high Sb(III) oxidation capacity through an indirect process. The CSB650 showed a stronger Sb(III)oxidation capacity as compared to CSB500 (Fig. 9 A), which might be related to its high EAC and oxidative metallic elements. First, CSB650 possessed more electron-accepting moieties (mainly carbonyl and quinone), which could capture the electrons in Sb(III) during the interaction between biochar and Sb, thus directly promoting the oxidation. Second, the higher contents of Fe and Mn were noted in CSB650 (Table S1), which might be another reason for its stronger oxidation capacity for Sb(III), as compared to CSB500. In a previous study, the presence of Fe and Mn in biochar was found to be responsible for As(III) oxidation, as reported by Dong et al. (2014), which might have a similar contribution to the Sb(III) oxidation in this study.

As discussed above, Sb(III) oxidation was mainly influenced by the PFRs and EEC of biochar. The reason for the greatest oxidation capacity of low-temperature derived CSB350 could be its highest EDC through indirect oxidation. Another possible pathway of direct oxidation to Sb(V) by $\bullet O_2^-$ and •OH cannot be excluded. As for the high-temperature pyrolyzed biochar, CSB650 had the highest EAC and concentrations of Fe and Mn, and the Sb(III) oxidation mechanism was majorly governed by the direct oxidation process.

4 Conclusions

Our results demonstrated that crawfish shell-derived biochar (CSB) can effectively remove Sb(III) from aqueous solution, and simultaneously reduce the toxicity of Sb by oxidizing Sb(III) to Sb(V). Therein, CSB pyrolyzed at 350°C (CSB350) possessed the highest adsorption capacity for Sb(III); and the maximum adsorption was found to be 27.7 mg g^{-1}. Batch adsorption and characterization results revealed the mechanisms for Sb(III) removal by CSB350 involved electrostatic interaction between $Sb(OH)_2^+$ and negative biochar surface under strongly acid condition, surface complexation with oxygen-containing functional groups, π–π coordination with aromatic groups, and hydrogen bonding with hydroxyl groups. Density functional theory calculations showed that O = C–O and C = O groups had the highest adsorption energy (AE= -2.94 eV and AE= -1.81 eV), highlighting the key role of surface complexation in Sb(III) adsorption. Moreover, CSB350 exhibited the strongest oxidation for Sb(III), and 78% of Sb(III) was oxidized to Sb(V), which might be due to its higher concentration of persistent free radicals and electron-donating capacity (0.128 mmol e^- (g biochar)$^{-1}$). Desorption and regeneration experiments indicated that CSB350 was a feasible adsorbent with robust stability for Sb(III) and great reusability performance. Overall, crawfish shell-derived biochar can be an environmentally-friendly and efficient adsorbent for the remediation of Sb(III) contaminated water. Future studies are needed to investigate the potential influence of crawfish shell biochar on the bioavailability and phytoavailability of Sb in the more complex soil-plant systems.

Supplementary information The online version contains supplementary material available at https://doi.org/10.1007/s42773-022-00161-2.

Author contributions **Hanbo Chen**: conceptualization, data curation, investigation, visualization, writing—original draft. **Yurong Gao**: data curation, investigation, writing—review and editing. **Jianhong Li**: data curation, writing—review and editing. **Chenghua Sun**: data curation, writing—review and editing. **Binoy Sarkar**: writing—review and editing. **Amit Bhatnagar**: writing—review and editing. **Nanthi Bolan**: writing—review and editing. **Xing Yang**: writing—review and editing. **Jun Meng**: writing—review and editing. **Zhongzhen Liu**: writing—review and editing. **Hong Hou**: writing—review and editing. **Jonathan W.C. Wong**: writing—review and editing. **Deyi Hou**: writing—review and editing. **Wenfu Chen**: conceptualization, writing—review and editing. **Hailong Wang**: conceptualization, supervision, writing—review and editing.

Funding This study was financially supported by the National Key Research and Development Program of China (2020YFC1807704), the National Natural Science Foundation of China (21876027), and the Science and Technology Innovation Project of Foshan, China (1920001000083). The authors acknowledge the Beijing Synchrotron Radiation Facility (BSRF, China) for providing the beam time of 1W1B and 4W1B. We also acknowledge Prof. Xinde Cao and his team at School of Environmental Science and Engineering, Shanghai Jiao Tong University, for their valuable helps on EDC/EAC analysis.

Availability of data and materials The datasets generated during and/or analyzed during the current study are available from the corresponding author on reasonable request.

Declarations

Conflict of interest The authors have no conflicts of interest to disclose, financial or otherwise.

References

Altaf AR, Adewuyi YG, Teng HP et al (2022) Elemental mercury (Hg^0) removal from coal syngas using magnetic tea-biochar: Experimental and theoretical insights. J Environ Sci 122:150–161

Altaf AR, Teng HP, Gang L et al (2021a) Effect of sonochemical treatment on thermal stability, elemental mercury (Hg^0) removal, and regenerable performance of magnetic tea biochar. ACS Omega 6:23913–23923

Altaf AR, Teng HP, Zheng MS et al (2021b) One-step synthesis of renewable magnetic tea-biochar derived from waste tea leaves for the removal of Hg^0 from coal-syngas. J Environ Chem Eng 9:105313

Bolan NS, Hoang SA, Beiyuan J et al (2022a) Multifunctional applications of biochar beyond carbon storage. Int Mater Rev 67:150–200

Bolan NS, Kumar M, Singh E et al (2022b) Antimony contamination and its risk management in complex environmental settings: A review. Environ Int 158:106908

Capra L, Manolache M, Ion I et al (2018) Adsorption of Sb (III) on oxidized exfoliated graphite nanoplatelets. Nanomaterials 8:992

Chen H, Feng Y, Yang X et al (2022a) Assessing simultaneous immobilization of lead and improvement of phosphorus availability through application of phosphorus-rich biochar in a contaminated soil: A pot experiment. Chemosphere 296:133891

Chen H, Gao Y, El-Naggar A et al (2022b) Enhanced sorption of trivalent antimony by chitosan-loaded biochar in aqueous solutions: Characterization, performance and mechanisms. J Hazard Mater 425:127971

Chen H, Gao Y, Li J et al (2022c) Engineered biochar for environmental decontamination in aquatic and soil systems: A review. Carbon Res. https://doi.org/10.1007/s44246-022-00003-7

Chen H, Qin P, Yang X et al (2021) Sorption of diethyl phthalate and cadmium by pig carcass and green waste-derived biochars under single and binary systems. Environ Res 193:110594

Chen H, Yang X, Wang H et al (2020a) Animal carcass- and wood-derived biochars improved nutrient bioavailability, enzyme activity, and plant growth in metal-phthalic acid ester co-contaminated soils: A trial for reclamation and improvement of degraded soils. J Environ Manage 261:110246

Chen S, Jiang S, Jiang H (2020b) A review on conversion of crayfish-shell derivatives to functional materials and their environmental applications. J Bioresour Bioprod 5:238–247

China Crawfish Industry Development Report (2019) China Fisheries 09:12–19 (in Chinese)

Cui X, Ni Q, Lin Q et al (2017) Simultaneous sorption and catalytic oxidation of trivalent antimony by *Canna indica* derived biochars. Environ Pollut 229:394–402

Delley B (1990) An all-electron numerical method for solving the local density functional for polyatomic molecules. J Chem Phys 92:508–517

Delley B (2000) From molecules to solids with the DMol3 approach. J Chem Phys 113:7756

Dong X, Ma L, Gress J et al (2014) Enhanced Cr(VI) reduction and As(III) oxidation in ice phase: important role of dissolved organic matter from biochar. J Hazard Mater 267:62–70

Habte L, Shiferaw N, Thriveni T et al (2020) Removal of Cd(II) and Pb(II) from wastewater via carbonation of aqueous Ca(OH)(2) derived from eggshell. Process Saf Environ 141:278–287

Hammer B, Hansen LB, Nørskov JK (1999) Improved adsorption energetics within Density-Functional Theory using revised Perdew-Burke-Ernzerh of functionals. Phys Rev B 59:7413–7421

Han L, Sun H, Ro KS et al (2017) Removal of antimony(III) and cadmium(II) from aqueous solution using animal manure-derived hydrochars and pyrochars. Bioresour Technol 234:77–85

Hu B, Ai Y, Jin J, Hayat T, Alsaedi A, Zhuang L, Wang X (2020) Efficient elimination of organic and inorganic pollutants by biochar and biochar-based materials. Biochar 2:47–64

Huang S, Xu C, Shao Q et al (2018a) Sulfide-modified zerovalent iron for enhanced antimonite sequestration: Characterization, performance, and reaction mechanisms. Chem Eng J 338:537–549

Huang P, Ge C, Feng D, Yu H, Luo J, Li J, Strong PJ, Sarmah AK, Bolan NS, Wang H (2018b) Effects of metal ions and pH on ofloxacin sorption to cassava residue-derived biochar. Sci Total Environ 616–617:1384–1391

Ji J, Xu S, Ma Z et al (2022) Trivalent antimony removal using carbonaceous nanomaterial loaded with zero-valent bimetal (iron/copper) and their effect on seed growth. Chemosphere 296:134047

Jia X, Zhou J, Liu J et al (2020) The antimony sorption and transport mechanisms in removal experiment by Mn-coated biochar. Sci Total Environ 724:138158

Klüpfel L, Keiluweit M, Kleber M et al (2014) Redox properties of plant biomass-derived black carbon (Biochar). Environ Sci Technol 48:5601–5611
Li L, Lai C, Huang F et al (2019) Degradation of naphthalene with magnetic bio-char activate hydrogen peroxide: Synergism of biochar and Fe/Mn binary oxide. Water Res 160:238–248
Li Q, Hu X, Hao J et al (2020) Characterization of Cu distribution in clay-sized soil aggregates by NanoSIMS and micro-XRF. Chemosphere 249:126143
Liu J, Zhou B, Zhang H et al (2019) A novel Biochar modified by Chitosan-Fe/S for tetracycline adsorption and studies on site energy distribution. Bioresour Technol 294:122152
Liu Z, Xu Z, Xu L et al (2022) Modified biochar: Synthesis and mechanism for removal of environmental heavy metals. Carbon Res. https://doi.org/10.1007/s44246-022-00007-3
Lv S, Xia C, Yang Q et al (2020) Improvements on high-temperature stability, rheology, and stiffness of asphalt binder modified with waste crayfish shell powder. J Clean Prod 264:121745
Ma J, Huang W, Li Y et al (2021) The utilization of lobster shell to prepare low-cost biochar for high-efficient removal of copper and cadmium from aqueous: Sorption properties and mechanisms. J Environ Chem Eng 9:104703
Ma S, Bao X, Yang Q et al (2019) Analysis on the research and application status of crayfish shell in China. Feed Res 493:95–97
Nie T, Yang X, Chen H et al (2021) Effect of biochar aging and coexistence of diethyl phthalate on the mono-sorption of cadmium and zinc to biochar-treated soils. J Hazard Mater 408:124850
Nishad PA, Bhaskarapillai A (2021) Antimony, a pollutant of emerging concern: A review on industrial sources and remediation technologies. Chemosphere 277:130252
Palansooriya KN, Kim S, Igalavithana AD et al (2021) Fe(III) loaded chitosan-biochar composite fibers for the removal of phosphate from water. J Hazard Mater 415:125464
Pan H, Yang X, Chen H et al (2021) Pristine and iron-engineered animal- and plant-derived biochars enhanced bacterial abundance and immobilized arsenic and lead in a contaminated soil. Sci Total Environ 763:144218
Park J, Wang J, Xiao R et al (2018) Effect of pyrolysis temperature on phosphate adsorption characteristics and mechanisms of crawfish char. J Colloid Interface Sci 525:143–151
Qin P, Wang H, Yang X et al (2018) Bamboo- and pig-derived biochars reduce leaching losses of dibutyl phthalate, cadmium, and lead from co-contaminated soils. Chemosphere 198:450–459
Rahman MA, Lamb D, Rahman MM et al (2021) Removal of arsenate from contaminated waters by novel zirconium and zirconium-iron modified biochar. J Hazard Mater 409:124488
Rajapaksha AU, Chen SS, Tsang DCW et al (2016) Engineered/designer biochar for contaminant removal/immobilization from soil and water: Potential and implication of biochar modification. Chemosphere 148:276–291
Rusmin R, Sarkar B, Liu Y et al (2015) Structural evolution of chitosan-palygorskite composites and removal of aqueous lead by composite beads. Appl Surf Sci 353:363–375
Salam MA, Mohamed RM (2013) Removal of antimony(III) by multi-walled carbon nanotubes from model solution and environmental samples. Chem Eng Res Des 91:1352–1360
Song J, Messele SA, Meng L et al (2021) Adsorption of metals from oil sands process water (OSPW) under natural pH by sludge-based Biochar/Chitosan composite. Water Res 194:116930
Sun T, Xu Y, Sun Y et al (2021) Crayfish shell biochar for the mitigation of Pb contaminated water and soil: Characteristics, mechanisms, and applications. Environ Pollut 271:116308
Vithanage M, Rajapaksha AU, Ahmad M et al (2015) Mechanisms of antimony adsorption onto soybean stover-derived biochar in aqueous solutions. J Environ Manage 151:443–449
Wan S, Liu L, Li Y et al (2020) Accelerated antimony and copper removal by manganese oxide embedded in biochar with enlarged pore structure. Chem Eng J 402:126021
Wang L, Wang J, Wang Z et al (2018) Enhanced antimonate (Sb(V)) removal from aqueous solution by La-doped magnetic biochars. Chem Eng J 354:623–632
Wei D, Li B, Luo L et al (2020) Simultaneous adsorption and oxidation of antimonite onto nano zero-valent iron sludge-based biochar: Indispensable role of reactive oxygen species and redox-active moieties. J Hazard Mater 391:122057
Wei J, Tu C, Yuan G et al (2019a) Carbon-coated montmorillonite nanocomposite for the removal of chromium(VI) from aqueous solutions. J Hazard Mater 368:541–549
Wei S, Zhu M, Fan X et al (2019b) Influence of pyrolysis temperature and feedstock on carbon fractions of biochar produced from pyrolysis of rice straw, pine wood, pig manure and sewage sludge. Chemosphere 218:624–631
Wen E, Yang X, Chen H et al (2021) Iron-modified biochar and water management regime-induced changes in plant growth, enzyme activities, and phytoavailability of arsenic, cadmium and lead in a paddy soil. J Hazard Mater 407:124344
Wu P, Wang Z, Bolan NS et al (2021) Visualizing the development trend and research frontiers of biochar in 2020: a scientometric perspective. Biochar 3(4):419–436
Wu T, Sun Q, Fang G et al (2019) Unraveling the effects of gallic acid on Sb(III) adsorption and oxidation on goethite. Chem Eng J 369:414–421
Xi J, He M, Wang K et al (2013) Adsorption of antimony(III) on goethite in the presence of competitive anions. J Geochem Explor 132:201–208
Xiao Y, Xue Y, Gao F et al (2017) Sorption of heavy metal ions onto crayfish shell biochar: effect of pyrolysis temperature, pH and ionic strength. J Taiwan Inst Chem Eng 80:114–121
Xiong N, Wan P, Zhu G et al (2020) Sb(III) removal from aqueous solution by a novel nano-modified chitosan (NMCS). Sep Purif Technol 236:116266
Xu Z, Xu X, Zhang Y et al (2020) Pyrolysis-temperature depended electron donating and mediating mechanisms of biochar for Cr(VI) reduction. J Hazard Mater 388:121794
Yang J, Pan B, Li H et al (2016) Degradation of pnitrophenol on biochars: role of persistent free radicals. Environ Sci Technol 50:694–700
Yang X, Hinzmann M, Pan H et al (2022) Pig carcass-derived biochar caused contradictory effects on arsenic mobilization in a contaminated paddy soil under fluctuating controlled redox conditions. J Hazard Mater 421:126647
Yang X, Pan H, Shaheen SM et al (2021) Immobilization of cadmium and lead using phosphorus-rich animal-derived and iron-modified plant-derived biochars under dynamic redox conditions in a paddy soil. Environ Int 156:106628
Yang X, Zhou T, Ren B et al (2017) Synthesis, characterization, and adsorptive properties of Fe_3O_4/GO nanocomposites for antimony removal. J. Anal. Methods Chem. 3012364
Yin G, Tao L, Chen X et al (2021) Quantitative analysis on the mechanism of Cd^{2+} removal by $MgCl_2$-modified biochar in aqueous solutions. J Hazard Mater 420:126487
Yu T, Wang X, Li C (2014) Removal of antimony by $FeCl_3$-modified granular-activated carbon in aqueous solution. J Environ Eng 140:A4014001
Zeng Z, Ye S, Wu H et al (2019) Research on the sustainable efficacy of g-MoS_2 decorated biochar nanocomposites for removing tetracycline hydrochloride from antibiotic-polluted aqueous solution. Sci Total Environ 648:206–217
Zhang C, Wang W, Duan A et al (2019a) Adsorption behavior of engineered carbons and carbon nanomaterials for metal endocrine

disruptors: Experiments and theoretical calculation. Chemosphere 222:184–194
Zhang D, Zhang K, Hu X et al (2021) Cadmium removal by $MgCl_2$ modified biochar derived from crayfish shell waste: Batch adsorption, response surface analysis and fixed bed filtration. J Hazard Mater 408:124860
Zhang Y, Xu X, Zhang P et al (2019b) Pyrolysis-temperature depended quinone and carbonyl groups as the electron accepting sites in barley grass derived biochar. Chemosphere 232:273–280
Zhou M, Wu Q, Wu H et al (2021) Enrichment of trace elements in red swamp crayfish: Influences of region and production method, and human health risk assessment. Aquaculture 535:736366
Zhu G, Lin J, Yuan Q et al (2021) A biochar supported magnetic metal organic framework for the removal of trivalent antimony. Chemosphere 282:131068

Authors and Affiliations

Hanbo Chen[1,2,3] · Yurong Gao[1,2,3] · Jianhong Li[1] · Chenghua Sun[4] · Binoy Sarkar[5] · Amit Bhatnagar[6] · Nanthi Bolan[7,8] · Xing Yang[1] · Jun Meng[2,3] · Zhongzhen Liu[9] · Hong Hou[10] · Jonathan W.C. Wong[11] · Deyi Hou[12] · Wenfu Chen[2] · Hailong Wang[1,2,13]

✉ Hailong Wang
hailong.wang@fosu.edu.cn

[1] School of Environmental and Chemical Engineering, Foshan University, 528000 Foshan, Guangdong, China

[2] Agronomy College, Shenyang Agricultural University, 110866 Shenyang, China

[3] Key Laboratory of Biochar and Soil Improvement, Ministry of Agriculture and Rural Affairs, 110866 Shenyang, China

[4] Department of Chemistry and Biotechnology, Center for Translational Atomaterials, Swinburne University of Technology, 3122 Hawthorn, VIC, Australia

[5] Future Industries Institute, University of South Australia, Mawson Lakes, SA 5095, Australia

[6] Department of Separation Science, LUT School of Engineering Science, LUT University, Sammonkatu 12, FI-50130 Mikkeli, Finland

[7] School of Agriculture and Environment, The University of Western Australia, 6001 Perth, WA, Australia

[8] The UWA Institute of Agriculture, The University of Western Australia, 6001 Perth, WA, Australia

[9] Institute of Agricultural Resources and Environment, Guangdong Academy of Agricultural Sciences, 510640 Guangzhou, China

[10] State Key Laboratory of Environmental Criteria and Risk Assessment, Chinese Research Academy of Environmental Sciences, 100012 Beijing, China

[11] Department of Biology, Hong Kong Baptist University, Kowloon Tong, Hong Kong SAR, China

[12] School of Environment, Tsinghua University, 100084 Beijing, China

[13] Guangdong Green Technologies Co., Ltd, 528100 Foshan, China